Laser & Photonics Reviews

LASER & PHOTONICS REVIEWS

www.lpr-journal.org

RESEARCH ARTICLE OPEN ACCESS

Bayesian Optimization of Grayscale Patterns for Layer-Height Accuracy in Projection Multi-Photon 3D Printing

Jason E. Johnson | Xianfan Xu

School of Mechanical Engineering and Birck Nanotechnology Center, Purdue University, West Lafayette, Indiana, USA

Correspondence: Xianfan Xu (xxu@ecn.purdue.edu)

Received: 26 January 2026 | **Revised:** 4 April 2026 | **Accepted:** 9 April 2026

Keywords: 3D printing | artificial intelligence | Bayesian optimization | grayscale digital light processing | machine learning | multi-photon polymerization | projection multi-photon lithography

ABSTRACT

Projection multi-photon lithography (PMPL) is a high-throughput, layer-by-layer nanoscale 3D printing method that can offer orders-of-magnitude higher fabrication speed than conventional direct laser writing techniques. Achieving precise geometric accuracy with PMPL requires accurate control of both in-plane patterning and the height of each printed layer, both of which are strongly affected by nonlinear polymerization kinetics and optical exposure conditions. We present a Bayesian optimization framework that integrates grayscale patterning with in situ quantitative phase imaging to autonomously correct layer-height deviations during PMPL. A simplified mechanistic model of the projection and polymerization process is incorporated, providing a physics-informed parameterization of grayscale exposure. Then, both the model's key parameters and specific process variables for grayscale patterning are optimized by the Bayesian framework to minimize layer-height error. Tests on representative 2D structures demonstrate that the method achieves more uniform, accurate layers in under 300 prints, substantially reducing experimental effort compared with conventional trial-and-error approaches. By integrating physics-informed parameterization, in situ optical metrology, and data-efficient machine learning, this approach enables precise and repeatable layers in PMPL and provides a broadly applicable strategy for optimization of other micro- and nano-fabrication processes.

1 | Introduction

Additive manufacturing at the micro- and nanoscale has become a critical enabling technology for applications ranging from micro-optics and photonics [1–3] and mechanical metamaterials [4–6] to microscale biomedical devices [7, 8]. Light-based 3D printing methods are particularly attractive at these length scales, as they can provide high-speed non-contact processing, truly three-dimensional patterning freedom, and resolution and feature sizes beyond the diffraction limit [9]. Among these approaches, multi-photon lithography (MPL), also called two-photon polymerization, has emerged as a versatile platform for fabricating complex 3D microstructures [10, 11]. Ongoing efforts in MPL increasingly focus on improving both throughput and geometric accuracy by understanding and tailoring the optical and photochemical processes that govern multi-photon polymerization.

In MPL, a high-peak-intensity ultrafast laser is tightly focused to induce multi-photon absorption in a photosensitive resin. The nonlinear intensity dependence of this process confines photopolymerization to a small focal volume, enabling sub-micron resolution and feature sizes [12, 13]. This same confinement, however, limits volumetric printing rates. Recent efforts in MPL

have focused on improving this throughput by parallelizing the printing process. This has been achieved by increasing the number of foci through use of metalens arrays [14], diffractive optical elements [15], and holography [16]. Projection multi-photon lithography (PMPL) is another recently developed approach that addresses this limitation by printing entire layers of a structure simultaneously, increasing volumetric printing rates by several orders of magnitude over single-point line scanning [17, 18].

Projection-based printing methods have long been used at the macro-scale [19, 20], but they typically rely on interfacial printing, which avoids the issue of intensity hot-spots away from the image plane, an issue inherent to coherent optical imaging. PMPL avoids sacrificing the truly three-dimensional design freedom of MPL by employing spatiotemporal focusing of ultrafast laser pulses. In this approach, a digital micromirror device (DMD) provides spatial amplitude modulation while its diffractive properties disperse the spectral components of the laser pulse, temporally stretching it. A 4f imaging system then recombines these components at the image plane, restoring a short pulse duration and enabling high-speed, layer-wise printing with sub-micron axial confinement.

PMPL therefore lies at a unique intersection between serial MPL and macro-scale projection-based 3D printing methods. Many of the challenges associated with projection-based approaches, such as image blurring due to diffraction and shape-dependent process parameters, are also present within PMPL [21]. However, these effects occur at much smaller length scales, approaching those of oxygen and photoinitiator diffusion, which are known to strongly influence MPL processes [22, 23]. Furthermore, the spatiotemporal focusing and 1D dispersion from the DMD produce a complicated 4D intensity profile (three spatial dimensions plus time) unique to each layer [23]. Together, these factors give rise to a complex process parameter space unique to PMPL, often necessitating time-consuming trial-and-error optimization for a given structure.

Pre-compensation methods have become an important tool for improving geometric accuracy in micro- and nanoscale 3D printing [24–27]. In the context of MPL, these approaches typically involve iteratively refining input designs or process parameters using simplified physical models and feedback measurements, often leveraging the fact that systematic deviations can be linked to local optical and photochemical processes at the voxel scale. In projection-based printing, similar pre-compensation concepts have been explored, but the simultaneous polymerization of an entire layer introduces additional challenges, including spatially varying exposure conditions and shape-dependent interactions [23, 28–30]. As a result, data-driven and machine-learning-based pre-compensation strategies have increasingly been explored, both in MPL [31–33] and projection-based additive manufacturing [34–36] to enable more flexible, adaptive, and generalizable pre-compensation strategies.

In PMPL, accurate fabrication requires control over both in-plane exposure and the effective height of each printed layer. Layer-height errors can accumulate over multiple layers, leading to significant geometric deviations despite good lateral pattern accuracy. Recent reaction-diffusion modeling work has shown that these errors arise from oxygen inhibition and diffusion and optical exposure nonuniformity and that there are promising routes for correction [23]. The shape dependence of these interactions, however, makes them difficult to correct using fixed process parameters or simple pre-compensation rules. While full reaction-diffusion models can provide useful physical insight, their usefulness is often limited by computational cost. Conversely, purely data-driven approaches typically require a large number of experiments.

Bayesian optimization provides a highly effective alternative that bridges this gap by efficiently navigating complex, black-box experimental spaces without the need for exhaustive parameter sweeps [37]. Unlike more common machine learning techniques, such as deep learning, which often require large datasets to achieve reliable convergence [38, 39], Bayesian optimization utilizes a probabilistic surrogate model to balance the exploration of uncertain parameter regions with the exploitation of known favorable conditions. In the context of PMPL, we have previously demonstrated that Bayesian optimization can achieve superior 2D geometric accuracy with four to five times less experimental data compared to convolution neural network-based approaches [21].

To leverage this efficiency for layer-height control, this work introduces a Bayesian framework that combines physics-informed parameterization, in situ measurement, and data-efficient optimization. First, a simplified mechanistic grayscale pattern generation method is developed to parameterize the projection exposure in terms of a small set of physically interpretable input parameters. Layer-height deviations are then measured using in situ quantitative phase imaging, providing consistent output metrics for evaluating layer accuracy. These input and output parameters are integrated within a Bayesian optimization framework that autonomously explores the process space to minimize layer-height error. The performance of the framework is demonstrated on representative two-dimensional layer structures, showing convergence to more uniform and accurate layers with substantially reduced experimental effort.

2 | Parameterization of Projection Multi-Photon Lithography

2.1 | Mechanistic Grayscale Pattern Generation

Grayscale exposure strategies provide a practical means of controlling photopolymerization by adjusting the local optical dose delivered to a resin. In digital light processing (DLP) systems, this concept is implemented by varying the time-averaged illumination intensity across the projected image, allowing spatial control over crosslink density during curing [40, 41]. Such approaches have been used to tune mechanical and functional material properties [42, 43], as well as to improve dimensional accuracy and effective resolution in DLP [30]. Although these methods are typically developed for macroscale DLP platforms, their underlying principles are relevant to PMPL, which similarly relies on DMD-based projection.

Applying grayscale patterning to PMPL introduces both opportunities and challenges that differ from those encountered in

conventional grayscale DLP (g-DLP) systems. One advantage is that the projected DMD pixels are strongly demagnified at the printing plane and are significantly smaller than the diffraction-limited spot size, enabling fine spatial control of exposure. However, PMPL operates with ultrafast pulsed laser illumination at relatively low repetition rates, rather than continuous-wave sources. Because the DMD provides only binary amplitude modulation, grayscale exposure for g-DLP and PMPL must be achieved by projecting sequences of binary patterns whose cumulative dose approximates the desired grayscale distribution. During continuous, high-speed layer printing in PMPL, individual patterns may receive only a small number of pulses and are projected at different axial positions within the resin. As a result, the effective polymerization produced by a given grayscale pattern depends on a combination of optical exposure conditions, polymerization kinetics, and process parameters, making direct determination of suitable patterns nontrivial. To address this challenge, a simplified mechanistic model is used to relate projected binary patterns to an estimated printed heightmap, providing a physics-informed basis for grayscale pattern generation. The objective of this approach is to estimate the printed result of a binary DMD pattern and to generate a compensating grayscale pattern that corrects deviations relative to the target layer geometry prescribed by the original binary pattern.

The optical intensity distribution within PMPL can be efficiently and accurately calculated using a Fourier optics model of the projection system [18, 23]. While detailed reaction-diffusion models of multi-photon polymerization have been reported [23], their computational cost inhibits their use in iterative pattern generation. Instead, the dominant effects of oxygen inhibition and diffusion are approximated by convolving the dose distribution with a Gaussian kernel [24, 44]. Assuming two-photon absorption is the dominant initiation mechanism, the normalized dose distribution $\hat{D}$ corresponding to a given 4D intensity distribution I, obtained from a Fourier optics model of the projection system [18, 23], is given by,

$$D\ (x,y,z) = \int_0^T I(x,y,z,t)^2 dt\ ,\ \hat{D} = \frac{D - \min(D)}{\max(D) - \min(D)} \quad (1)$$

where T is the exposure period. The 2D printed layers studied in this work are printed on the substrate surface. This surface influences the reaction-diffusion process by acting as a no-flux boundary for diffusion processes, reducing oxygen inhibition near the substrate [23]. This effect can be approximated during the Gaussian-kernel-convolution [24] process by using an asymmetric kernel along the z-axis,

$$K\ (x,y,z;\sigma) = \frac{1}{(2\pi)^{3/2}\sigma^3}\ \exp\left(-\frac{x^2+y^2+z^2}{2\sigma^2}\right) H(-z)\,, \quad (2)$$

where σ is the sole free parameter of the kernel and represents an effective diffusion length scale and $H(-z)$ is the Heaviside function causing the upper half of the kernel to be zero. Then by only padding the upper portion of the dose during the numerical convolution process, diffusion-limited polymerization on the substrate can be reasonably approximated. The output polymerization heightmap P is then simply the maximum z value that the Gaussian filtered normalized dose exceeds a threshold value τ or,

$$P\ (x,y;\tau) = \max_z \left\{ \left(\hat{D} \otimes K\right) \geq \tau \right\}\ , \quad (3)$$

where $\otimes$ denotes a convolution operation. This max{·} operation reduces the mechanistic model results down to the 2D grayscale image space. The threshold τ is a tunable parameter, but $\tau = 19.5\%$ was found to work well for all results in this work.

Figure 1 shows the different components of the grayscale pattern generation method. Figure 1a shows the printed result measured by quantitative phase imaging [45] for an unmodified 6.75 × 6.75 μm single binary butterfly pattern. Figure 1b provides an example of the prediction of a printed layer for the same 6.75 μm binary butterfly pattern. The 3D normalized dose distribution calculated by the Fourier optics model (shown after thresholding at 19.5% only for visualization purposes) exhibits an irregular distribution with prominent features along the top and bottom but softer edges along the sides due to 1D dispersion of the DMD [23]. The asymmetric kernel is shown with a cutout for visualization purposes and is not to scale. Convolving the dose with a $\sigma = 0.8$ μm kernel and thresholding with $\tau = 19.5\%$ yields a simulated layer with smooth features that closely approximates the experimentally measured result in Figure 1a.

Once a heightmap has been calculated from Equation), a grayscale error map can be generated by subtracting the normalized simulated heightmap from the normalized target heightmap. An example error map is shown in Figure 1c. This error map serves as the starting point for the grayscale pattern. From here, several further variations can be made. The grayscale error map predicts the undesired effects of inhibition and diffusion during projection of the binary pattern. To account for these same processes during the projection of the grayscale compensation patterns, a diffusion compensation parameter, α, can be defined as,

$$I_{out}\ (\alpha) = \frac{I_{in}}{(1-\alpha) + \alpha\,(I_{in} \otimes K)}\ , \quad (4)$$

where I_{in} is the input grayscale pattern, I_{out} is the diffusion-compensated grayscale pattern, and K is now a 2D Gaussian kernel with the same effective diffusion length σ used during generation of the grayscale error map [46]. Scaling the grayscale error map by the inverse of its Gaussian-blurred self leads to increased brightness at the edges and around smaller features, where under-polymerization due to oxygen diffusion will be greater. The degree of compensation for diffusion/oxygen inhibition during projection of the grayscale pattern can then be controlled by adjusting α between zero and one, where zero is no compensation, and one is full compensation. Figure 1d shows the diffusion-compensated pattern for the error map in Figure 1c with $\sigma = 0.8$ μm and $\alpha = 1$. Lastly, the nonlinearity of the grayscale pattern can be adjusted using the common gamma correction operation, or $I_{out} = I_{in}^{\gamma}$, where γ is the nonlinearity parameter. This is used to further tune this difference in exposure between darker and brighter portions of the pattern.

Once the grayscale compensation image has been generated, it must be converted into a sequence of binary patterns for

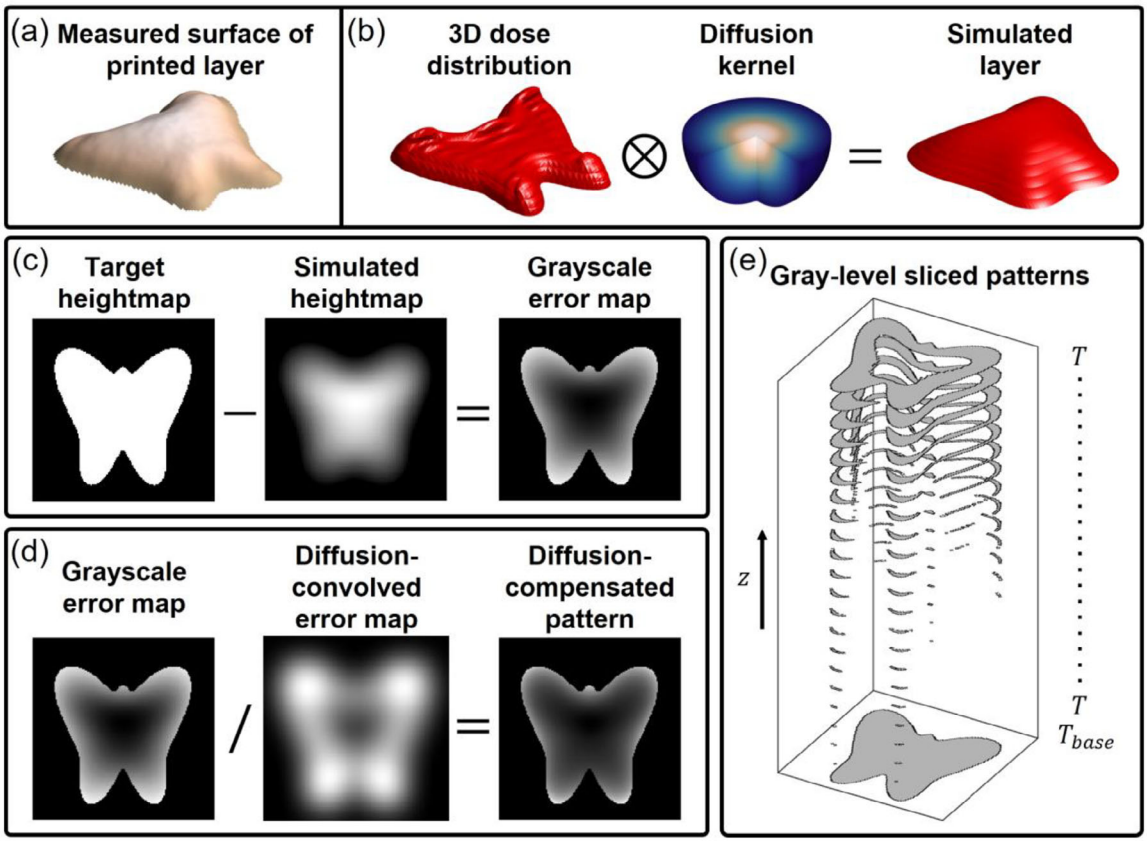

FIGURE 1 | Grayscale pattern generation method. (a) Printed result for binary 6.75 μm butterfly pattern, measured using quantitative phase imaging. (b) Mechanistic-model-based layer prediction. The 3D dose distribution, computed via a Fourier optics model, for a binary butterfly pattern is convolved with the bottom half of a Gaussian kernel to predict a polymerized layer on the substrate surface. A heightmap is generated by removing all polymerization less than 19.5%. (c) A grayscale error map is generated by subtracting the normalized simulated height map from the target layer height map. (d) The diffusion-limited effects during projection of the grayscale pattern can be compensated for by scaling the grayscale error map by the inverse of its diffusion-convolved self. (e) The resulting grayscale pattern is then sliced such that the original binary pattern is projected for a period of $\boldsymbol{T_{base}}$ and then a sequence of compensation patterns is each projected for a period of $\boldsymbol{T}$.

projection on the DMD. While conventional grayscale DLP often relies on bit-plane slicing, this approach is poorly suited for PMPL due to the limited temporal sampling inherent to pulsed, high-speed projection. Bit-plane slicing produces granular, high-spatial-frequency binary patterns that can lead to polymerization artifacts when only a small number of laser pulses are delivered per pattern during continuous motion. To avoid these effects, this work employs a linear slicing strategy in which the grayscale intensity range is divided into n_{pat} linearly spaced levels, and a binary pattern is generated for each level by thresholding the grayscale image. Prior to slicing, all nonzero pixels are rescaled such that the lowest slice corresponds to the original binary pattern used to generate the simulated heightmap, referred to here as the base pattern. This base pattern is projected with an exposure duration T_{base}, while the remaining $n_{pat}-1$ slice acts as a compensation patterns and is projected with a separate exposure duration T for each pattern. These compensation patterns are ordered such that larger-area patterns are projected later in the sequence, farther from the substrate, where greater compensation is typically required. An example of the gray-level sliced patterns generated from the result in Figure 1d is shown in Figure 1e. The grayscale pattern generation parameters used in this work and their optimization ranges are summarized in Table 1.

2.2 | In Situ Quantitative Phase Imaging for Layer-Height Measurement

In situ quantitative phase imaging (QPI) is used to measure the printed layer geometry during PMPL without removal and development of the sample, thereby significantly increasing the throughput of the optimization method. QPI provides a spatial map of the optical phase delay introduced by the printed structure, which is directly related to the accumulated optical path length through the polymerized material. In this work, phase maps are reconstructed from a set of intensity images acquired at multiple defocus planes using the transport-of-intensity equation (TIE), which relates the axial derivative of intensity to the transverse Laplacian of the optical phase [45]. For a weakly absorbing, predominantly phase object with slowly varying intensity, like a thin polymer printed layer, the TIE can be approximated as,

$$\frac{\partial}{\partial z}I = -\frac{\lambda}{2\pi}I_0\nabla_\perp^2\phi, \tag{5}$$

where I is the measured intensity, I_0 is the in-focus intensity, ϕ is the optical phase, λ is the illumination wavelength, and $\nabla_\perp$ is the transverse gradient. Approximating the intensity derivative with multiple defocus images equally spaced above and below the focal

TABLE 1 | Input parameter descriptions.

Input parameter	Range	Description
w	±1.25 μm	Maximum width of the projected shape
h	±1.25 μm	Maximum height of the projected shape
σ	[0.001, 1.5] μm	Effective diffusion length of the Gaussian kernel
γ	[0.2,5]	Gamma correction nonlinearity parameter
α	[0,1]	Diffusion compensation parameter
n_{pat}	[0,22]	Number of binary patterns for grayscale image slicing
T_{base}	[398,1198] μs	Exposure period of the first, base pattern
T	[398,1598] μs	Exposure period of remaining compensation patterns

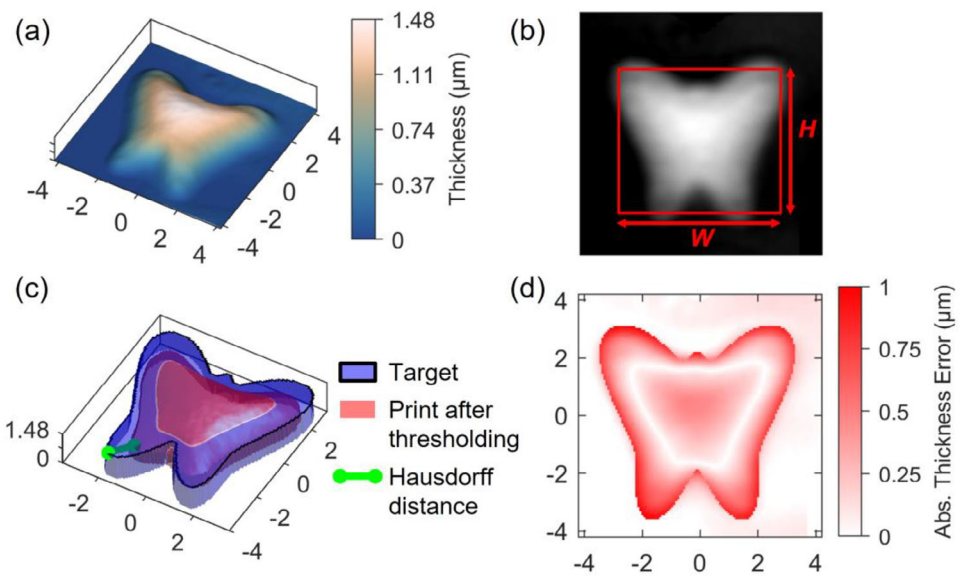

FIGURE 2 | Quantitative-phase-imaging-based output metrics. (a) Surface plot of heightmap measured with quantitative phase imaging. (b) Width and height measurements taken from the bounding box of the heightmap after Otsu-thresholding. (c) Hausdorff distance is measured between the target shape and the printed result after thresholding. (d) Color plot of absolute thickness error between the target shape and the printed result. The total volume of this error divided by the top area of the target provides the mean thickness error metric.

plane, denoising using the optimal frequency selection method [47], and solving this equation yields a smooth quantitative phase map of the printed layer [45]. For thin printed layers, the measured phase delay can be interpreted as layer thickness through the relation $t = \phi\lambda/2\pi\Delta n$, where Δn is the refractive index difference between polymerized and unpolymerized resin. In the context of PMPL in this work, where the target geometry for each layer is nominally planar, this 2.5D measurement is sufficient to quantify deviations from the desired layer thickness.

Figure 2 summarizes the QPI-derived output metrics used in this work. The measured phase maps are converted into layer-thickness heightmaps, from which scalar error metrics are extracted to guide optimization. Figure 2a shows a heightmap of a printed result for a 6.75 μm binary butterfly pattern. For this work, four metrics are measured from this heightmap relative to a target geometry: width error ΔW, height error ΔH, Hausdorff distance d_H, and mean thickness error ε_t. These metrics are straightforward extensions of the 2D shape metrics used in previous work [21] to the present 2.5D QPI measurements. The width and height are taken from the bounding box of the shape after Otsu-thresholding. The bounding box for the heightmap in Figure 2a is shown in Figure 2b. The Hausdorff distance was computed between the 3D point clouds extracted from the measured and target heightmaps. This metric captures the largest local deviation between the printed and target structures, providing a measure of the worst-case surface mismatch. This typically occurs between the upper edge of the printed and target shapes and can therefore be thought of as an edge sharpness measurement. Extracting a point cloud for this measurement requires that a boundary be defined for the printed shape. Therefore, the measurement is performed after Otsu-thresholding. This thresholding process inherently favors sharper printed edges for planar targets. Softer edges will have more material below the threshold thickness removed, leading to poor printed dimensions. As edges become sharper and closer to the target shape, less printed material is below the threshold thickness, leading to less removal during thresholding and more accurate

TABLE 2 | Output metric descriptions.

Output metric	Unit	Description
W	μm	Maximum width of printed shape after thresholding
H	μm	Maximum height of printed shape after thresholding
d_H	μm	Hausdorff distance between the target surface and the printed surface after Otsu-thresholding. Typically serves as an edge sharpness metric.
ε_t	μm	Mean thickness error, computed by taking the absolute error volume between the printed and target surfaces and dividing by the area of the top target surface.

printed dimensions. For non-planar targets, a more rigorous edge detection method may be necessary to avoid removing more subtle (softer edge) boundaries. Figure 2c shows the Hausdorff distance in green between the 1 μm thick target shape (blue) and the Otsu-thresholded print (red). Finally, Figure 2d shows the absolute thickness error map between the 1 μm thick target and the printed result. The mean thickness error is computed by taking the volume of this error and dividing by the area of the target surface. This metric serves as a measurement of the overall quality of the printed geometry. Table 2 lists the output metrics, their units, and their descriptions. Because QPI measurements can be acquired rapidly and non-destructively after each printed layer, these metrics provide an efficient and reliable output for closed-loop Bayesian optimization of grayscale exposure parameters.

2.3 | Bayesian Optimization Framework

Bayesian optimization (BO) is well-suited for optimizing experimental processes that are expensive to evaluate and exhibit stochastic variability [37]. For optimization of geometric accuracy in 3D printing, each evaluation corresponds to a full print and measure cycle, and the process parameter spaces are typically large and strongly coupled, making exhaustive parameter sweeps often impractical. BO addresses this challenge by combining a probabilistic surrogate model with an acquisition strategy that sequentially selects new experiments to efficiently explore the parameter space in order to improve a chosen objective. In this work, BO is used to minimize layer-height error by adaptively tuning the grayscale pattern generation parameters described in Section 2.1 based on in situ QPI metrics introduced in Section 2.2. The framework presented here is based on previous work, where additional details on Bayesian optimization can be found [21]. The framework is implemented within Python using the Ax open-source platform [48].

The surrogate model is constructed using Gaussian process (GP) regression. A GP defines a distribution over functions, such that any finite set of function values follows a multivariate normal distribution. For an input parameter vector $\mathbf{x}$, the latent response function $f(\mathbf{x})$ is modeled as

$$f(\mathbf{x}) \sim \mathcal{GP}(m(\mathbf{x}), k(\mathbf{x}, \mathbf{x}')), \tag{6}$$

where $m(\mathbf{x})$ is the mean function and $k(\mathbf{x}, \mathbf{x}')$ is the covariance function [37]. The choice of the mean and covariance functions controls the shape of the distribution predicted by the GP. Experimental observations are assumed to be noisy measurements of this latent function,

$$y = f(\mathbf{x}) + \varepsilon, \tag{7}$$

where y is the experimental observation and $\varepsilon \sim \mathcal{N}(0, \sigma_n^2)$ is the experimental noise, which follows a zero-mean normal distribution with variance σ_n^2. Conditioning the GP on observed data yields a posterior prediction distribution characterized by a mean $\mu(\mathbf{x})$ and variance $\sigma^2(\mathbf{x})$, which together quantify both the predicted result for a given input parameter set and the uncertainty of the model for that predicted result. In this work, independent single-task (one output) GP models are used for each of the four QPI output metrics, and each model has a constant mean function and a radial basis covariance function (RBF) [37]. The four predicted output metrics are then combined into one scalar metric via a weighted summation of the normalized values, or $U(\mathbf{x}) = -\sum_{i=1}^{n} w_i \bar{\mu}_i(\mathbf{x})$, where μ_i is the model's predicted mean for the i^{th} output metric. A negative sum is used because the objective of this work is to minimize error, but BO is typically treated as a maximization problem. Since the metrics used here are strongly positively correlated, any minor tradeoffs can be tuned via the weights w_i. For metrics that exhibit stronger tradeoffs, or where a suitable w_i is not easily determined, optimization of the Pareto frontier [37] can be easily implemented in the Ax platform, where the optimal tradeoff is learned during optimization. This, however, slows optimization due to the additional computational cost.

The acquisition function governs the selection of the next parameter set to experimentally observe by using the GP posterior to balance exploration and exploitation. This work uses an acquisition function based on the commonly used Expected Improvement (EI) function, defined as

$$\text{EI}(\mathbf{x}) = \mathbb{E}[\max\{0, U(\mathbf{x}) - U^*\}] \tag{8}$$

where $\mathbb{E}$ is the expectation operator and U^* is the best observed value thus far. This expression can be evaluated analytically under the GP posterior and naturally favors parameter regions with either low predicted error or high uncertainty. In this study, two acquisition functions are used. The Parallel Log Noisy Expected Improvement, or qLogNEI [49], serves as the primary acquisition function for identifying the next best experiments to run to improve the model. The qLogNEI function is based on Expected Improvement but implements several changes to improve numerical performance. The Parallel Simple Regret, or qSR [37], is used to evaluate the performance of the current model by selecting points within the parameter space that the model expects to perform well, regardless of the uncertainty. The parallel or "q" in each of these names denotes the use of parallel candidate acquisition. The GP formulation allows for efficient parallel computations, but calculation of expectation within the acquisition function is no longer closed form, therefore

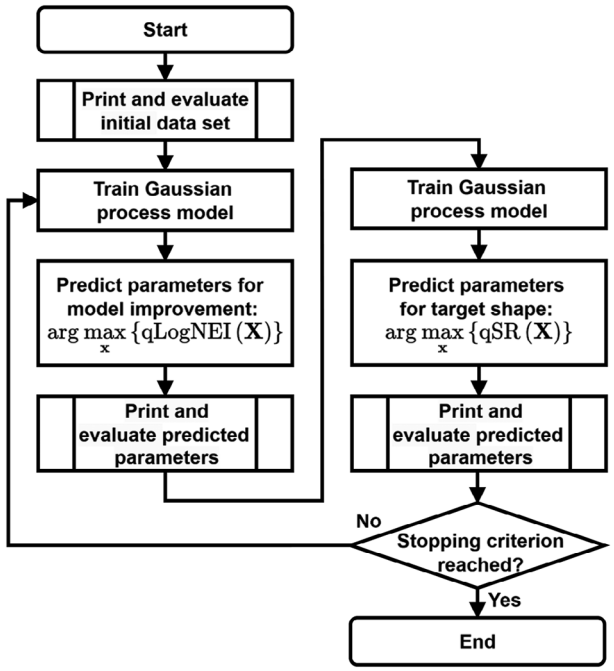

FIGURE 3 | Flowchart for the Bayesian optimization framework.

the solution is approximated via Monte Carlo sampling from the GP model's predicted posterior [49]. The complexity of these acquisition functions highlights the benefits of the Ax platform, in that they can be easily implemented without rigorous derivations.

Figure 3 illustrates the overall Bayesian optimization workflow developed in this study. The process begins with the collection of an initial training dataset consisting of 24 quasi-random grayscale pattern samples uniformly distributed across the input parameter space defined in Section 2.1, a single point centered within the domain, and a small number of user-defined manual sampling locations. These manual samples, typically four to eight per optimization run, are chosen based on prior experience or from favorable parameter sets previously identified through trial-and-error and serve to accelerate early model convergence. A Gaussian process surrogate model is then trained using all available data and used to inform the qLogNEI acquisition function. The candidates returned by the acquisition function are experimentally evaluated through printing and in situ QPI measurement, after which the resulting metrics described in Section 2.2 are added to the training set. The model is retrained and used to inform the qSR acquisition function. These additional candidates are similarly printed and measured. The optimization then iterates between EI-driven exploration and regret-driven exploitation until a stopping criterion is met. A number of stopping criteria can be used, but for this work, the optimization process is simply stopped after 300 prints, as suitable convergence and result quality were consistently observed within this number of iterations.

3 | Results

The framework was used to optimize layer accuracy for five different 1 μm thick target shapes. The target layer height of 1 μm was selected because it is near the minimum axial feature size achievable with PMPL [18] and therefore represents a stringent test case for layer-height control, though the framework itself is not restricted to this target thickness. A 6.75 μm square, circle, and right isosceles triangle were optimized for demonstration on simple representative shapes and a 6.75 μm butterfly and 13.5 × 6.75 μm Purdue-P logo were optimized for demonstration on more complex shapes. For each shape, the following parameters in Table 1, were optimized by the model: w, h, σ, γ, T_{base}, and T. For the simple shapes, no diffusion compensation was used, or α =0, and the number of patterns was fixed at n_{pat} = 12. For the butterfly and Purdue logo, diffusion compensation was necessary to achieve uniform thickness across the more complex geometry, as these compensation patterns contain more features of varying size and spacing that experience different levels of diffusion-limited polymerization. Therefore, α was fixed at 1, and n_{pats} was optimized by the model. While optimization of all parameters for each shape is feasible, using prior knowledge to fix certain parameters helps increase the efficiency of optimization.

For all shapes, the negative weighted sum of the four normalized output parameters, or $U(\mathbf{x})$, was maximized. Weights of $\mathbf{w} = [1, 1, 5, 10]$ were assigned respectively to the output parameters, $[\Delta W, \Delta H, d_H, \varepsilon_t]$. These were determined via trial-and-error. Since the Hausdorff distance and mean thickness error exhibit asymptotic behavior above zero while the width and height errors can approach zero, larger weights for the former two metrics helps avoid local minima where the width and height errors are very small, but shape quality is poor. To better evaluate the impact of grayscale pattern optimization, some baseline results were gathered using only binary patterns. For these binary results, the model optimized the binary target pattern's exposure period and the z-axis translation speed during exposure to try and achieve a 1 μm thick layer. For all grayscale prints, the z-axis translation speed was calculated so that the total duration of all patterns occurred within the target thickness of 1 μm. The optimization results for each shape for binary and grayscale patterning are shown in Table 3. For ΔW and ΔH, a negative value means undersized, and a positive value means oversized. The optimal grayscale patterning parameters determined by the framework and used to obtain the results in Table 3, are shown in Table 4.

The optimization results for the 6.75 μm butterfly are shown in Figure 4. The results for the Purdue-P, square, circle, and triangle are shown in Figures S1–S4, respectively. Figure 4a,c show the surface plot of the QPI measurement for the optimal binary patterning and optimal grayscale patterning results, respectively. The color bar for these plots is scaled from zero to the maximum thickness, and the target thickness of 1 μm is bolded. Figure 4b,d show a color plot of the thickness error, or the difference between the target heightmap and the printed heightmap, for the binary and grayscale patterning results. The color bar for the thickness error map in each of these figures is scaled from −1 μm to 1 μm to provide a to-scale comparison between results. Negative thickness error occurs when the printed result is thinner than the target, and positive thickness error occurs when the printed result is thicker than the target. The maximum and minimum thickness error for each result is labeled on the color bar and bolded. The optimal grayscale pattern and an ordered and expanded view of its binary slices are shown in Figure 4e,f.

TABLE 3 | Optimization results for binary and grayscale patterning.

	ΔW		ΔH		d_H		ε_t	
Shape	**Binary [μm]**	**Grayscale [μm]**	**Binary [μm]**	**Grayscale [μm]**	**Binary [μm]**	**Grayscale [μm]**	**Binary [μm]**	**Grayscale [μm]**
Butterfly	−0.54	−0.057	1.23	−0.057	1.221	0.381	0.389	0.230
Purdue-P	−0.873	0.024	0.012	0.012	0.946	0.710	0.313	0.249
Square	−0.678	0.081	−0.471	0.081	0.941	0.416	0.287	0.197
Circle	−0.816	−0.057	−0.609	0.012	0.681	0.377	0.283	0.193
Triangle	−1.437	−0.057	−1.437	0.081	1.451	0.466	0.369	0.318

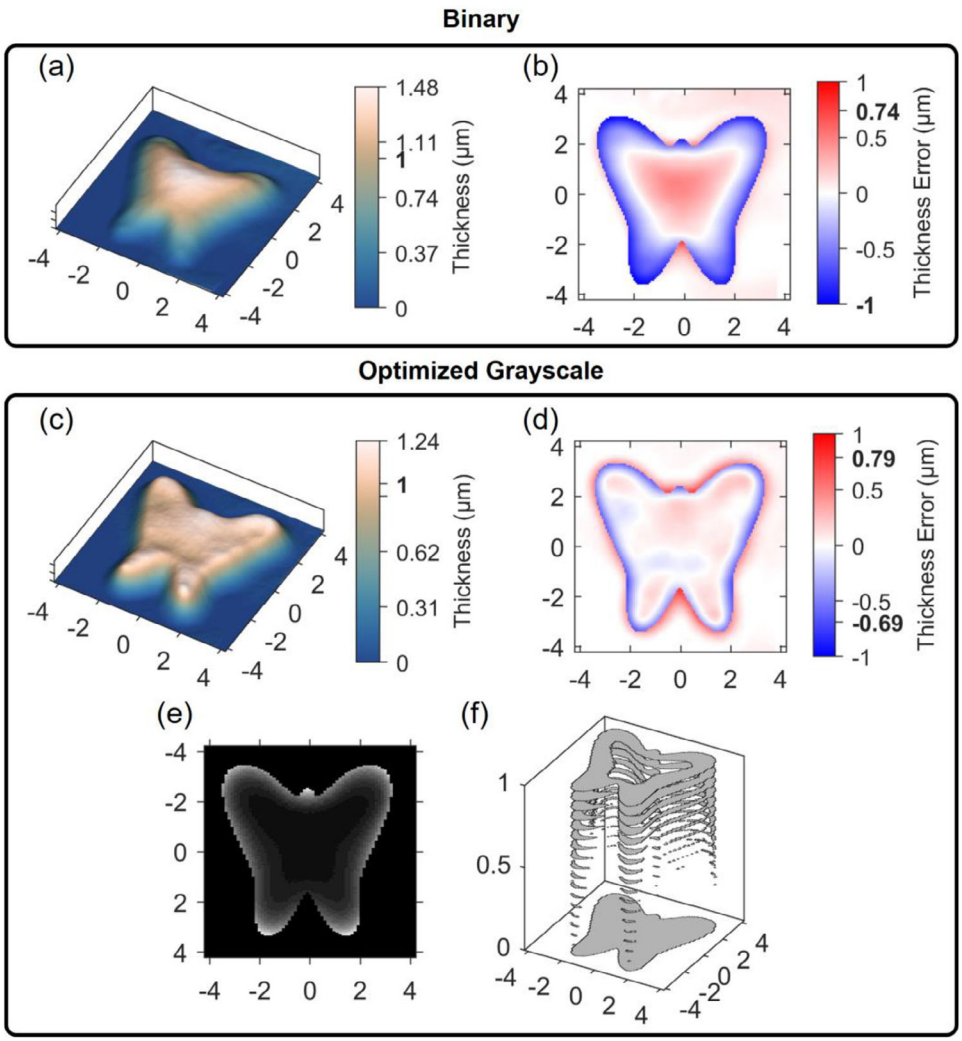

FIGURE 4 | Optimization results for 6.75 μm butterfly shape. All axes are in units of μm. (a) Surface plot of optimal result for binary patterning. The color bar is scaled from zero to the maximum thickness, with the target thickness of 1 μm bolded. (b) Color plot of thickness error for the binary patterning result. The color bar is scaled from −1 μm to 1 μm. The minimum and maximum errors are labeled in bold. (c) Surface plot of optimal result for grayscale patterning. (d) Color plot of thickness error for the grayscale patterning result. (e) Optimal grayscale pattern. (f) Expanded view of binary slices of optimal grayscale pattern.

4 | Discussion and Conclusions

These results demonstrate that grayscale patterning provides substantial improvement over binary patterning alone. The optimization framework consistently achieves sub-100 nm accuracy in both the width and height of the printed layers, with the Hausdorff distance reduced by an average of 580 nm, from approximately 1.05 μm for binary patterns to 470 nm for grayscale patterns. By comparison, the reduction in mean thickness error

TABLE 4 | Optimal grayscale patterning parameters.

Shape	w [µm]	h [µm]	σ [µm]	γ	T_{base} [µs]	T [µs]	n_{pat}	α
Butterfly	6.760	6.833	0.878	1.572	598	610	18	1
Purdue-P	13.966	6.738	1.039	1.558	598	424	22	1
Square	7.020	7.003	0.496	2.339	637	398	12	0
Circle	6.843	6.945	0.423	2.932	598	684	12	0
Triangle	7.494	7.614	0.301	3.208	598	487	12	0

TABLE 5 | Inner and outer error of binary and grayscale results.

	Inner Error		Outer Error	
Shape	Binary [µm]	Grayscale [µm]	Binary [µm]	Grayscale [µm]
Butterfly	0.334	0.142	0.047	0.075
Purdue-P	0.254	0.146	0.062	0.103
Square	0.270	0.113	0.026	0.091
Circle	0.266	0.118	0.020	0.072
Triangle	0.327	0.157	0.031	0.088

is more modest. However, inspection of the thickness error maps in Figure 4b,d, as well as Figures S1–S4, shows that despite the smaller numerical change, there is a clear qualitative improvement in layer uniformity and edge definition. This apparent discrepancy can be understood by separating the mean thickness error into inner and outer errors. Table 5 reports these values for both binary and grayscale results across all tested shapes. The inner error, defined as the mean thickness error within the target geometry, shows a stronger improvement for grayscale patterning, with average values near 130 nm, whereas binary results remain closer to the total mean thickness error. In contrast, the outer error, defined as the mean thickness outside the target boundary, is slightly larger for grayscale results. For binary patterns, width and height are not optimized, and edge sharpness remains diminished, resulting in minimal polymerization outside the target boundary. Grayscale optimization improves dimensional accuracy and edge sharpness, but proximity effects lead to increased polymerization around the target boundary, resulting in larger outer errors. All these tradeoffs are captured within the mean thickness error metric used in our BO framework, yielding a more subdued improvement relative to the other metrics. This behavior highlights a key advantage of separating print accuracy into multiple complementary metrics, which allows different tradeoffs to be explicitly quantified and weighted during optimization.

A variance-based Sobol sensitivity analysis (Note S2) was performed on the 6.75 µm butterfly surrogate model to evaluate the influence of the mechanistic pattern generation parameters on the printed layer geometry. The results reveal that the metrics are heavily impacted by the grayscale patterning parameters, specifically the effective diffusion length, nonlinearity factor, and number of binary patterns for grayscale slicing. Furthermore, the substantially larger total order indices compared to first-order indices for these variables indicate a highly coupled parameter space characterized by strong interactions. The complexity of this coupled parameter space demonstrates the need for machine learning-guided exploration.

As with any optimization problem, there is an inherent tradeoff between the number of degrees of freedom and computational efficiency. Several parameters in the framework, such as the dose threshold τ, were fixed based on prior observations that they performed well across all tested geometries. Other constraints arise from experimental and hardware limitations and represent clear opportunities for future improvement. All results in this work were obtained at a fixed laser power, as the current experimental setup does not support autonomous power control. A power of 270 mW (~135 W cm^{-2}) was chosen so that printing the ~6.75 µm binary base patterns at the minimum exposure period yields maximum layer thicknesses just below 1 µm, allowing the remaining patterns to focus entirely on compensation. Laser power directly influences the balance between edge sharpness and thickness uniformity: higher powers reduce oxygen inhibition for small features but increase the risk of over-polymerization in larger regions. Allowing the optimization framework to tune laser power alongside grayscale parameters may enable improved trade-offs. Similarly, the number of binary slices per grayscale pattern is limited by the DMD image buffer size and pattern switching time. Increasing the number of slices while reducing the minimum exposure duration per pattern would improve temporal resolution. Within existing hardware limits, additional flexibility could be achieved by extending the exposure model beyond the two exposure periods used here (T_{base} and T), enabling more refined temporal weighting of the grayscale compensation patterns.

Beyond the single-field, layer-wise demonstrations presented here, the framework naturally suggests pathways for extension to both larger-area and fully 3D structures. For lateral scaling, because diffusion-induced deviations are predominantly localized near the structure boundaries [21], the need for grayscale compensation remains mostly localized even for larger patterns. When stitching multiple fields, interface errors could be captured by the existing QPI metrics, meaning they could be directly addressed by the Bayesian framework by introducing a stitching overlap or spacing input parameter. Axially, although in situ QPI provides a phase map that does not uniquely determine the underlying 3D geometry, the measured phase profile still encodes integrated thickness and material distribution information that is highly relevant for optimization. In a fully 3D context, expected or target phase profiles could still provide meaningful optimization targets, allowing Bayesian optimization to correct systematic deviations even when the exact geometry is not uniquely observable. More generally, the combination of physics-informed parameterization, in situ optical metrology, and data-efficient optimization provides a flexible foundation that can be adapted to more complex geometries, alternative feedback signals, and additional process parameters.

In summary, this work demonstrates an autonomous machine-learning-based optimization framework for improving layer-height accuracy in projection multi-photon lithography by integrating mechanistic grayscale pattern generation, in situ quantitative phase imaging, and Bayesian optimization. Compared with

single-pattern binary exposure, the grayscale exposure strategy enables finer spatial control of dose delivery, allowing correction of thickness nonuniformity and systematic edge deviations that cannot be addressed using a single binary pattern per layer. Optimizing these grayscale parameters enables the Bayesian framework to achieve more uniform, sharper, and repeatable layers within 300 prints, substantially reducing experimental effort compared with manual tuning. Beyond PMPL, the framework provides a general strategy for closed-loop optimization in micro- and nanoscale additive manufacturing processes where physical models are incomplete, measurements are indirect, or experiments are costly.

5 | Experimental Section/Methods

The printing system was based on a Ti:sapphire regenerative amplifier (Coherent Legend Elite Duo USX) producing ∼50 fs pulses at a repetition rate of 5 kHz, with a center wavelength of 800 nm and a spectral bandwidth of approximately 30 nm. Laser power was adjusted using a half-wave plate (Thorlabs AHWP10M-580) in combination with a polarizing beam splitter cube (Thorlabs PBS25-780). The beam was collimated and expanded to an approximate diameter of 12 mm using a concave lens (f = −125 mm, Edmund Optics #49-539) followed by a convex lens (f = 150 mm, Thorlabs LA1417-B). To mitigate speckle effects in the projected beam during printing, a piezo-actuated tip–tilt mirror (PI S-330.8SL) was used to translate the beam in a circular pattern at high speed. The beam profile was converted from a Gaussian to a flattop intensity distribution using a beam-shaping optic (AdlOptica πShaper 12_12_TiS_HP). The shaped beam was then incident on a digital micromirror device (DLP4500NIR) at an angle of 24° relative to the surface normal.

Light diffracted from the DMD in the blazed mode along the surface normal was collected by an achromatic doublet (f = 180 mm, Thorlabs AC508-180-AB; CL in Figure S6) and focused at the back focal plane of the microscope objective lens (OL in Figure S6). A Nikon 100× objective with numerical aperture NA = 1.49 was used for printing and data collection. A dichroic mirror reflective over the wavelength range 760–840 nm (Eskma Optics, 045–800) redirected the printing beam by 90° while transmitting a helium-neon (He-Ne) laser used for focus detection.

For in situ imaging of the sample plane, a 50/50 beam splitter (Thorlabs BSW27; BS in Figure S6) was placed after the dichroic mirror and before the objective lens. The imaging path consisted of an imaging lens (f = 100 mm, Thorlabs LA1509-B; IL in Figure S6) and a CMOS camera (FLIR GS3-U3-32S4M). Sample positioning was controlled using a three-axis air-bearing translation stage (Aerotech ABL1000 series). The objective lens was immersed directly into the photoresist deposited on a precleaned microscope slide.

The photoresist used in this work was (2E,6E)-2,6-Bis (4-(dibutylamino) benzylidene)-4-methylcyclohexanone (BBK) mixed into the monomer pentaerythritol triacrylate (PETA) at 0.38 mol% [50]. BBK is a highly efficient Norrish Type II photoinitiator which, after undergoing multi-photon absorption, typically generates a radical via intermolecular hydrogen atom transfer with the monomer. This radical then reacts with the monomer, initiating free-radical chain growth. The exact mechanisms of this highly efficient BBK + PETA photoresist system are still an active area of research [23, 51].

Printing was automated through serial communication with the DMD controller using MATLAB and LabVIEW, with synchronized motion control implemented via Aerotech's Automation1 software. Fine axial positioning of the objective lens was achieved using a piezo-actuated stage (PI P-725.4CD). Prior to printing each sample, an automated focusing routine was executed in LabVIEW, in which the objective lens was positioned to bring the He-Ne laser into focus with an axial precision of ∼100 nm.

All samples were printed at a fixed laser power of 270 mW, which corresponds to an average intensity of ∼135 W cm^{-2} at the printing plane. After printing each sample, 61 images were recorded at different z-positions within a range of 12 μm with a step size of 200 nm. These images were processed to generate the quantitative phase map [45, 47]. A 660 nm LED (Thorlabs M660L3-C3) was used as the illumination source. The LED was collimated with a collimating lens, (f = 25 mm, Thorlabs LA1252; CoL in Figure S6). A 600 μm diameter aperture (A in Figure S6) was placed approximately 1 mm from the bottom of the substrate to provide sufficient coherence for quantitative phase imaging. Calculation of the phase map was performed in MATLAB using a refractive index of 1.517 for PETA and a $\Delta n = 0.025$ [45]. Measurement of the output metrics was performed in Python.

Acknowledgements

This work was supported by the National Science Foundation (NSF) through grant numbers CMMI-2135585 and CMMI-2229143. J.E.J. acknowledges the National Science Foundation for support under the Graduate Research Fellowship Program (GRFP) under grant number DGE-1842166. We thank the NSF for its gracious support. We thank Prof. Bryan Boudouris and Kaushik Baruah for the synthesis of the BBK photoinitiator.

Conflicts of Interest

The authors declare no conflicts of interest.

Data Availability Statement

The data and computer code supporting the results within this paper and other findings of the study are available from the corresponding authors upon reasonable request.

References

1. M. Farsari, "Advances in 3D and 4D Multi-Photon Printing for Micro and Nano Photonics [Invited]," *Optical Materials Express* 15 (2025): 2770–2791, https://doi.org/10.1364/OME.558798.

2. Y. Kang, J. Zhao, Y. Zeng, X. Du, and Z. Gu, "3D Printing Photonic Crystals: A Review," *Small* 20 (2024): 2403525, https://doi.org/10.1002/smll.202403525.

3. A. Zolfaghari, T. Chen, and A. Y. Yi, "Additive Manufacturing of Precision Optics at Micro and Nanoscale," *International Journal of Extreme Manufacturing* 1 (2019): 012005, https://doi.org/10.1088/2631-7990/ab0fa5.

4. R. Su, J. Chen, X. Zhang, et al., "3D-Printed Micro/Nano-Scaled Mechanical Metamaterials: Fundamentals, Technologies, Progress, Applications, and Challenges," *Small* 19 (2023): 2206391.

5. Z. Chen, Y.-T. Lin, H. Salehi, et al., "Advanced Fabrication of Mechanical Metamaterials Based on Micro/Nanoscale Technology," *Advanced Engineering Materials* 25 (2023): 2300750, https://doi.org/10.1002/adem.202300750.

6. Y. Wang, C. Yi, W. Tian, F. Liu, and G. J. Cheng, "Free-Space Direct Nanoscale 3D Printing of Metals and Alloys Enabled by Two-Photon Decomposition and Ultrafast Optical Trapping," *Nature Materials* 23 (2024): 1645–1653, https://doi.org/10.1038/s41563-024-01984-z.

7. K. Muldoon, Y. Song, Z. Ahmad, X. Chen, and M.-W. Chang, "High Precision 3D Printing for Micro to Nano Scale Biomedical and Electronic Devices," *Micromachines* 13 (2022): 642, https://doi.org/10.3390/mi13040642.

8. M. Rothbauer, C. Eilenberger, S. Spitz, et al., "Recent Advances in Additive Manufacturing and 3D Bioprinting for Organs-On-A-Chip and Microphysiological Systems," *Frontiers in Bioengineering & Biotechnology* 10 (2022): 837087.

9. P. Somers, A. Münchinger, S. Maruo, C. Moser, X. Xu, and M. Wegener, "The Physics of 3D Printing With Light," *Nature Reviews Physics* 6 (2024): 99–113, https://doi.org/10.1038/s42254-023-00671-3.

10. E. Skliutas, G. Merkininkaitė, S. Maruo, et al., "Multiphoton 3D Lithography," *Nature Reviews Methods* 5 (2025): 15.

11. S. Kawata, H.-B. Sun, T. Tanaka, and K. Takada, "Finer Features for Functional Microdevices," *Nature* 412 (2001): 697–698, https://doi.org/10.1038/35089130.

12. H. Wang, W. Zhang, D. Ladika, et al., "Two-Photon Polymerization Lithography for Optics and Photonics: Fundamentals, Materials, Technologies, and Applications," *Advanced Functional Materials* 33 (2023): 2214211.

13. X. Zhou, Y. Hou, and J. Lin, "A Review on the Processing Accuracy of Two-Photon Polymerization," *AIP Advances* 5 (2015): 030701, https://doi.org/10.1063/1.4916886.

14. S. Gu, C. Mao, A. Guell Izard, et al., "3D nanolithography With Metalens Arrays and Spatially Adaptive Illumination," *Nature* 648 (2025): 591–599.

15. P. Kiefer, V. Hahn, S. Kalt, et al., "A Multi-Photon (7 × 7)-Focus 3D Laser Printer Based on a 3D-Printed Diffractive Optical Element and a 3D-Printed Multi-Lens Array," *Light: Advanced Manufacturing* 4 (2024): 1–14.

16. L. Zhang, C. Wang, C. Zhang, et al., "High-Throughput Two-Photon 3D Printing Enabled by Holographic Multi-Foci High-Speed Scanning," *Nano Letters* 24 (2024): 2671–2679, https://doi.org/10.1021/acs.nanolett.4c00505.

17. S. K. Saha, D. Wang, V. H. Nguyen, Y. Chang, J. S. Oakdale, and S.-C. Chen, "Scalable Submicrometer Additive Manufacturing," *Science* 366 (2019): 105–109, https://doi.org/10.1126/science.aax8760.

18. P. Somers, Z. Liang, J. E. Johnson, B. W. Boudouris, L. Pan, and X. Xu, "Rapid, Continuous Projection Multi-photon 3D Printing Enabled by Spatiotemporal Focusing of Femtosecond Pulses," *Light: Science & Applications* 10 (2021): 199, https://doi.org/10.1038/s41377-021-00645-z.

19. J. R. Tumbleston, D. Shirvanyants, N. Ermoshkin, et al., "Continuous Liquid Interface Production of 3D Objects," *Science* 347 (2015): 1349–1352.

20. C. Sun, N. Fang, D. M. Wu, and X. Zhang, "Projection Micro-Stereolithography Using Digital Micro-Mirror Dynamic Mask," *Sensors and Actuators A: Physical* 121 (2005): 113–120, https://doi.org/10.1016/j.sna.2004.12.011.

21. J. E. Johnson, I. R. Jamil, L. Pan, G. Lin, and X. Xu, "Bayesian Optimization With Gaussian-Process-Based Active Machine Learning for Improvement of Geometric Accuracy in Projection Multi-Photon 3D Printing," *Light: Science & Applications* 14 (2025): 56, https://doi.org/10.1038/s41377-024-01707-8.

22. J. B. Mueller, J. Fischer, F. Mayer, et al., "Polymerization Kinetics in Three-Dimensional Direct Laser Writing," *Advanced Materials* 26 (2014): 6566–6571, https://doi.org/10.1002/adma.201402366.

23. A. I. Akash, J. E. Johnson, and X. Xu, "Modeling and Improving Geometric Accuracy in Projection Multiphoton Lithography," *Advanced Optical Materials* 14 (2026): 03185, https://doi.org/10.1002/adom.202503185.

24. N. Lang, S. Enns, J. Hering, and G. von Freymann, "Towards Efficient Structure Prediction and Pre-Compensation in Multi-Photon Lithography," *Optics Express* 30 (2022): 28805–28816, https://doi.org/10.1364/OE.462775.

25. H.-B. Sun, T. Suwa, K. Takada, et al., "Shape Precompensation in Two-Photon Laser Nanowriting of Photonic Lattices," *Applied Physics Letters* 85 (2004): 3708–3710, https://doi.org/10.1063/1.1807019.

26. G. Oguguo, A. Tanguy, S. Hallais, and L. Bodelot, "Characterization and Compensation of Distortions in Complex 3D Architected Microstructures Printed by Two-Photon Polymerization," *Journal of Manufacturing Processes* 149 (2025): 229–240, https://doi.org/10.1016/j.jmapro.2025.05.039.

27. J. Weinacker, S. Kalt, P. Kiefer, P. Rietz, and M. Wegener, "On Iterative Pre-Compensation of 3D Laser-Printed Micro-Optical Components Using Confocal-Optical Microscopy," *Advanced Functional Materials* 34 (2024): 2309356, https://doi.org/10.1002/adfm.202309356.

28. C. Wen, Z. Chen, Z. Chen, et al., "Improvement of the Geometric Accuracy for Microstructures by Projection Stereolithography Additive Manufacturing," *Crystals (Basel)* 12 (2022): 819, https://doi.org/10.3390/cryst12060819.

29. X. Wang, J. Liu, Y. Liu, et al., "High-precision and Large-Scale Vat Photopolymerization Printing Based on "Spatial-Pixel Integration Compensation" Method," *Additive Manufacturing* 92 (2024): 104351.

30. S. M. Montgomery, F. Demoly, K. Zhou, and H. J. Qi, "Level Grayscale Manipulation to Improve Accuracy in Digital Light Processing 3D Printing," *Advanced Functional Materials* 33 (2023): 2213252.

31. Y. Yang, V. A. Kelkar, H. S. Rajput, A. C. Salazar Coariti, K. C. Toussaint, and C. Shao, "Machine-Learning-Enabled Geometric Compliance Improvement in Two-Photon Lithography Without Hardware Modifications," *Journal of Manufacturing Processes* 76 (2022): 841–849, https://doi.org/10.1016/j.jmapro.2022.02.046.

32. S. Jia, J. Sun, A. Howes, M. R. Dawson, K. C. Toussaint, and C. Shao, "Hybrid Physics-Guided Data-Driven Modeling for Generalizable Geometric Accuracy Prediction and Improvement in Two-Photon Lithography," *Journal of Manufacturing Processes* 110 (2024): 202–210, https://doi.org/10.1016/j.jmapro.2023.12.024.

33. S. Enns, J. Hering-Stratemeier, and G. von Freymann, "First Steps towards Machine Learning for Prediction and Pre-Correction in Direct Laser Writing," *arXiv* (2025).

34. I. R. Jamil, J. E. Johnson, and X. Xu, "Convolutional Autoencoder Frameworks for Projection Multi-Photon 3D Printing," *Additive Manufacturing* 110 (2025): 104929.

35. B. Zhao, M. Zhang, L. Dong, and D. Wang, "Design of Grayscale Digital Light Processing 3D Printing Block by Machine Learning and Evolutionary Algorithm," *Composites Communications* 36 (2022): 101395, https://doi.org/10.1016/j.coco.2022.101395.

36. T. Poltue, S. M. Montgomery, X. Sun, et al., "Machine Learning-Based Optimization of Pixel Light Intensities for Improving Polymerization Accuracy in Digital Light Processing 3D Printing," *Advanced Materials Technology* 10 (2025): 00902.

37. R. Garnett, *Bayesian Optimization* (Cambridge University Press, 2023), https://doi.org/10.1017/9781108348973.

38. J. Hestness, S. Narang, N. Ardalani, et al., "Deep Learning Scaling Is Predictable Empirically," *arXiv* (2017), https://doi.org/10.48550/arXiv.1712.00409.

39. C. Wang, X. P. Tan, S. B. Tor, and C. S. Lim, "Machine Learning in Additive Manufacturing: State-of-the-Art and Perspectives," *Additive Manufacturing* 36 (2020): 101538.

40. G. I. Peterson, J. J. Schwartz, D. Zhang, et al., "Production of Materials With Spatially-Controlled Cross-Link Density via Vat Photopolymerization," *ACS Applied Materials & Interfaces* 8 (2016): 29037–29043, https://doi.org/10.1021/acsami.6b09768.

41. X. Kuang, J. Wu, K. Chen, et al., "Grayscale Digital Light Processing 3D Printing for Highly Functionally Graded Materials," *Science Advances* 5 (2025): aav5790, https://doi.org/10.1126/sciadv.aav5790.

42. L. Yue, S. M. Montgomery, X. Sun, et al., "Single-Vat Single-Cure Grayscale Digital Light Processing 3D Printing of Materials With Large Property Difference and High Stretchability," *Nature Communications* 14 (2023): 1251, https://doi.org/10.1038/s41467-023-36909-y.

43. J. Nam, B. Chen, and M. Kim, "Machine Learning-Driven Grayscale Digital Light Processing for Mechanically Robust 3D-Printed Gradient Materials," *Advanced Materials* 37 (2025): 2504075, https://doi.org/10.1002/adma.202504075.

44. E. H. Waller and G. Von Freymann, "Spatio-Temporal Proximity Characteristics in 3D μ-Printing via Multi-Photon Absorption," *Polymers (Basel)* 8 (2016): 297, https://doi.org/10.3390/polym8080297.

45. R. Zvagelsky, P. Kiefer, J. Weinacker, and M. Wegener, "In-situ Quantitative Phase Imaging During Multi-photon Laser Printing," *ACS Photonics* 10 (2023): 2901–2908, https://doi.org/10.1021/acsphotonics.3c00625.

46. V. Hahn, P. Rietz, F. Hermann, et al., "Light-Sheet 3D Microprinting via Two-Colour Two-Step Absorption," *Nature Photonics* 16 (2022): 784–791, https://doi.org/10.1038/s41566-022-01081-0.

47. C. Zuo, Q. Chen, Y. Yu, and A. Asundi, "Transport-of-Intensity Phase Imaging Using Savitzky-Golay Differentiation Filter—Theory and Applications," *Optics Express* 21 (2013): 5346–5362, https://doi.org/10.1364/OE.21.005346.

48. M. Olson, E. Santorella, and L. C. Tiao, "Ax: A Platform for Adaptive Experimentation," *AutoML* 293 (2025): 21/1–25.

49. S. Ament, S. Daulton, D. Eriksson, M. Balandat, and E. Bakshy, "Unexpected Improvements to Expected Improvement for Bayesian Optimization," in *Thirty-Seventh Conference on Neural Information Processing Systems* (2023), https://doi.org/10.52202/075280-0904.

50. P. Kiefer, V. Hahn, M. Nardi, et al., "Sensitive Photoresists for Rapid Multiphoton 3D Laser Micro- and Nanoprinting," *Advanced Optical Materials* 8 (2020): 2000895, https://doi.org/10.1002/adom.202000895.

51. A. Mauri, P. Kiefer, W. Wenzel, and M. Kozlowska, "Photoreactivity of Norrish Type Photoinitiators for 3D Laser Printing via First Principles Calculations," *Macromolecular Rapid Communications* 46 (2025): 2500231, https://doi.org/10.1002/marc.202500231.

Supporting Information

Additional supporting information can be found online in the Supporting Information section.

Supporting File: lpor71200-sup-0001-SuppMat.docx.